Supplementary materials

S.1 Determination of the bore duration.

In this study the bore length and period need to be determined from the experimental data and numerical results. The bore length is defined as the distance from the bore front to the beginning of the bore tail. Similarly, the bore period is defined as the time duration between the bore front reaches a certain location and the beginning of the tail crosses the same location.

For illustration, the time histories of dimensionless free surface elevations at CG2 for cases of $L_r/h_0 = 80$ and $F_{in} = 1.1, 1.3, 1.5$ and 1.9 are plotted in figures S1 - S4, respectively. Undulating bores (figures S1 and S2), undulating-breaking bores (figure S3) and breaking bores (figure S4), depending on the input bore strength, have very different surface profiles. In undulating and undulating-breaking bores the amplitudes of the surface converge towards the bore height in an oscillatory manner. Breaking bores have a steep front with wave breaking. In both undulating-breaking and breaking bores, relatively small fluctuations ride the bore plateau and the bore tail. The maximum bore height for undulating bores coincides with the leading wave crest. On the other hand, for undulating-breaking and breaking bores the maximum height may be found anywhere between the bore front and the beginning of the bore tail.

While it is straightforward to identify the arrival time of a bore and the maximum bore height, the identification of the beginning of the bore tail and therefore the bore period, is more challenging. This is specially true for shorter bores. For the present study, the arrival time of a bore is defined as the first instant when $\eta/h_0 > 0.02$. For some long bore cases the reflections from the slope reach the gauge before the end of the bore tail. These records have been truncated so that the reflections are not included in the bore analysis.

In figures S5 - S8 histograms of the free surface elevation records plotted in figures S1 - S4 are constructed. The bin size is 0.05 with 50% overlapping. The peak in the histograms represents the most repeated elevations, i.e., the bore plateau height. As shown in these figures, for a fixed reservoir length $L_r/h_0 = 80$ the dimensionless plateau height varies with the bore strength. The beginning of the bore tail for these cases is identified with the data point inside the bin of the bore plateau, which appears last in the time series. The bore period is calculated as the time difference between the bore arrival time and the beginning of the bore tail. In addition, the bore height is calculated as the average of the heights of all the points between the first height measurement equal to or larger than the height at the beginning of the tail and the beginning of the bore tail (circle and square markers in figures S1 - S4).

A similar procedure has been adopted to identify the beginning and end of the flooding plateau at the still water shoreline. To illustrate this, the time histories of the free surface elevation at the still water shoreline for $L_r/h_0 = 176$ and $F_{in} = 1.1, 1.3, 1.5$ and 1.9 are plotted in figures S9 to S12. The corresponding histograms are shown in figures S13 to S16. The beginning and end of the flooding plateau are identified with the first and last data point, after the maximum inundation depth, inside the bin of the flooding plateau.

S.2 Numerical model calibration.

To calibrate the numerical model, the free surface elevations obtained from the numerical simulations have been compared with the laboratory measurements. The comparisons are performed at the toe of the slope and the still water shoreline. Three cases with $L_r/h_0 = 80$ and different bore strength have been compared: non-breaking ($F_{in} = 1.1$

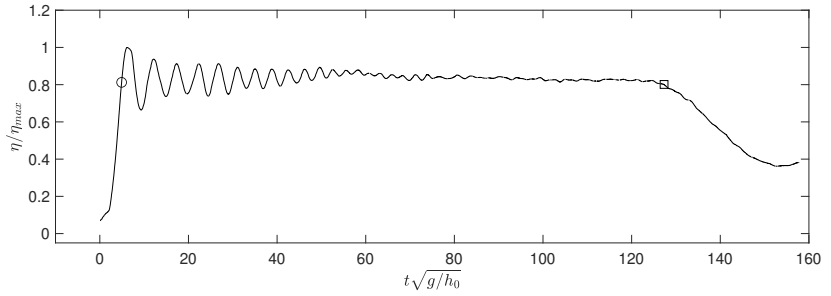

FIGURE S1. Time history of normalized free surface elevations at CG2 for $L_r/h_0 = 80$ and $F_{in} = 1.1$. The square marks the beginning of the bore tail and the circle the first point with the same amplitude.

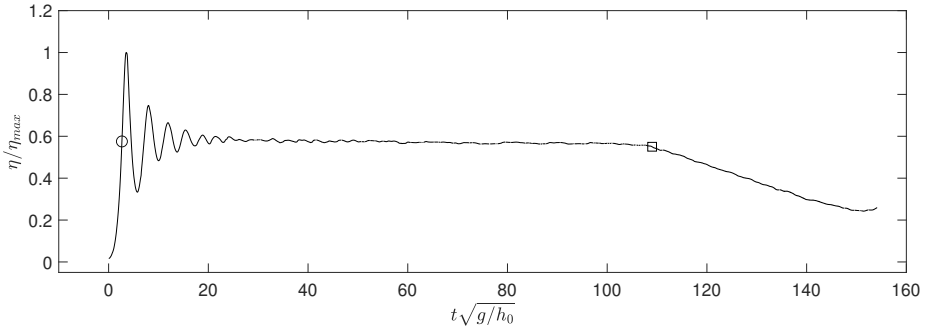

FIGURE S2. Time history of normalized free surface elevations at CG2 for $L_r/h_0 = 80$ and $F_{in} = 1.3$. The square marks the beginning of the bore tail and the circle the first point with the same amplitude.

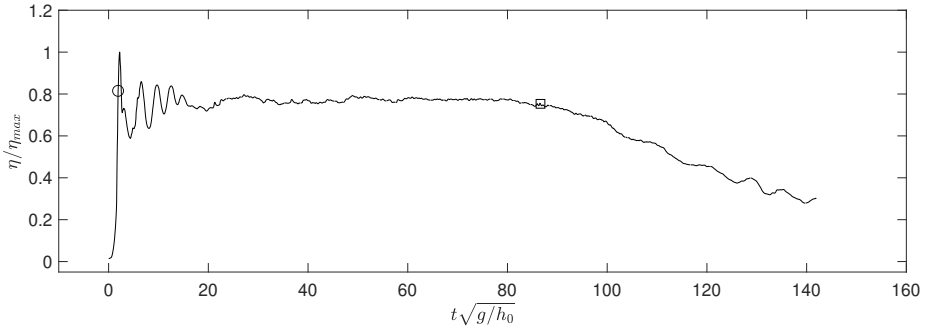

FIGURE S3. Time history of normalized free surface elevations at CG2 for $L_r/h_0 = 80$ and $F_{in} = 1.5$. The square marks the beginning of the bore tail and the circle the first point with the same amplitude.

& 1.2) and undulating-breaking ($F_{in} = 1.5$). Results for grid sizes $\Delta x = 0.01$ m, 0.02 m and 0.03 m and steepness values $0.4 < \delta < 1.2$ are compared to the laboratory results.

Numerical results for cases $F_{in} = 1.1$, $F_{in} = 1.2$ and $F_{in} = 1.5$ with $\delta = 0.8$, are compared to laboratory measurements in figures S17 - S22. For $F_{in} = 1.1$ and $F_{in} = 1.5$ no visible differences in the numerical results are observed for different grid sizes. For $F_{in} = 1.2$ the bore breaks before reaching the toe of the slope for $\Delta x = 0.01$m, producing a smaller inundation depths at the still water shoreline. The numerical results match well with the laboratory measurements for $\delta = 0.8$ and $\Delta x = 0.02$ m. It is observed that bores

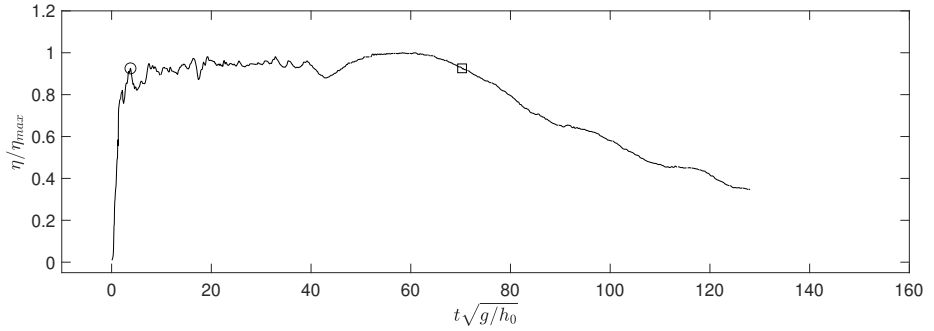

FIGURE S4. Time history of normalized free surface elevations at CG2 for $L_r/h_0 = 80$ and $F_{in} = 1.9$. The square marks the beginning of the bore tail and the circle the first point with the same amplitude.

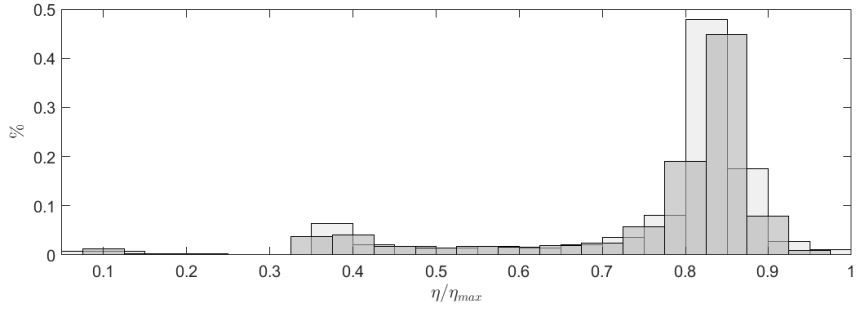

FIGURE S5. The histogram of normalized free surface elevations at CG2 (figure S1) for $L_r/h_0 = 80$ and $F_{in} = 1.1$.

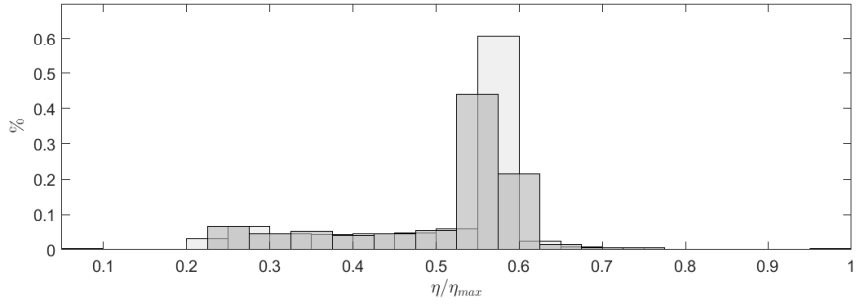

FIGURE S6. The histogram of normalized free surface elevations at CG2 (figure S2) for $L_r/h_0 = 80$ and $F_{in} = 1.3$.

break earlier for smaller δ and Δx values. On the other hand, for larger δ and Δx values, larger non-breaking undulations take place. Comparisons for $F_{in} > 1.5$, not shown, are similar to the comparisons for $F_{in} = 1.5$.

The analyses of mesh independence and δ calibration for the maximum inundation depth at the still water shoreline and the maximum runup heights are presented in figures S23, S24 and S25 for $F_{in} = 1.1$, 1.2 and 1.5, respectively. For all three cases, the numerical solutions converge to the laboratory measurements as the mesh size is reduced. However, larger δ values are required for small Δx to adjust the breaking in the

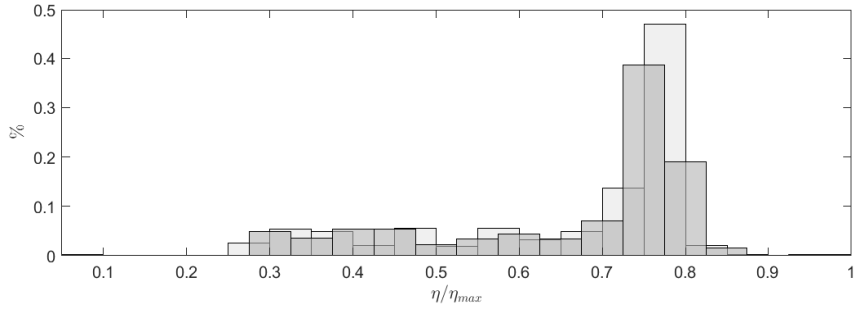

FIGURE S7. The histogram of normalized free surface elevations at CG2 (figure S3) for $L_r/h_0 = 80$ and $F_{in} = 1.5$.

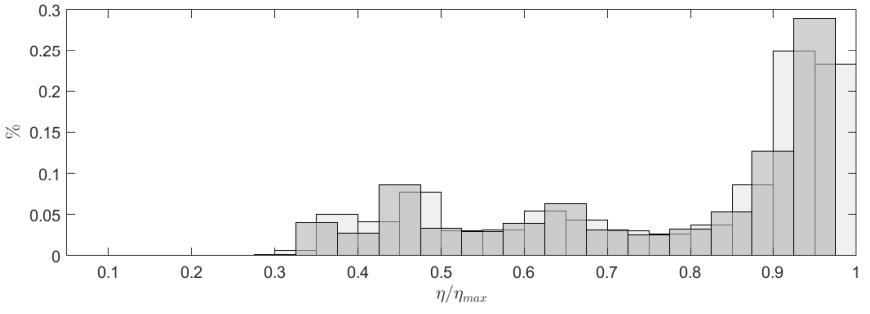

FIGURE S8. The histogram of normalized free surface elevations at CG2 (figure S4) for $L_r/h_0 = 80$ and $F_{in} = 1.9$.

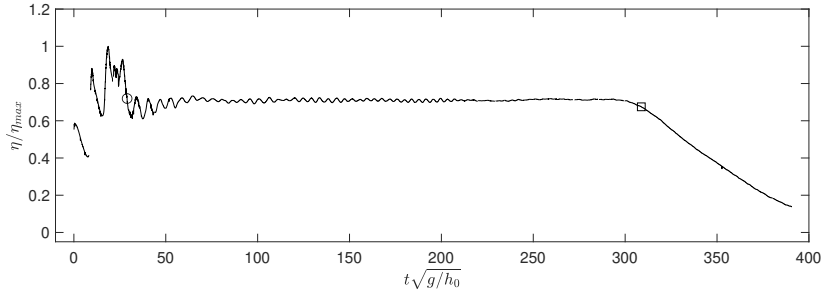

FIGURE S9. Time history of normalized free surface elevation at the still water shoreline for $L_r/h_0 = 176$ and $F_{in} = 1.1$. The circle and the square markers represent the beginning and end of the bore plateau.

numerical simulations. It is also clear that the convergence of numerical solutions is less sensitive to δ value for the case of $F_{in} = 1.5$.

In addition, the computational cost for each simulation, expressed as the time necessary to carry out the simulation (t_{num}) divided the simulation duration (t_{sim}), are also plotted in figures S23, S24 and S25. The computational cost grows exponentially for smaller grid sizes, and becomes notoriously more costly for $\Delta x < 0.02$ m. Based on the trade-off between the model accuracy and computational cost, it is considered an appropriate compromise to use the grid size $\Delta x = 0.02$ m to simulate the laboratory experiments and additional numerical simulations for h_0 and h_1/h_0 within the same range. Based on

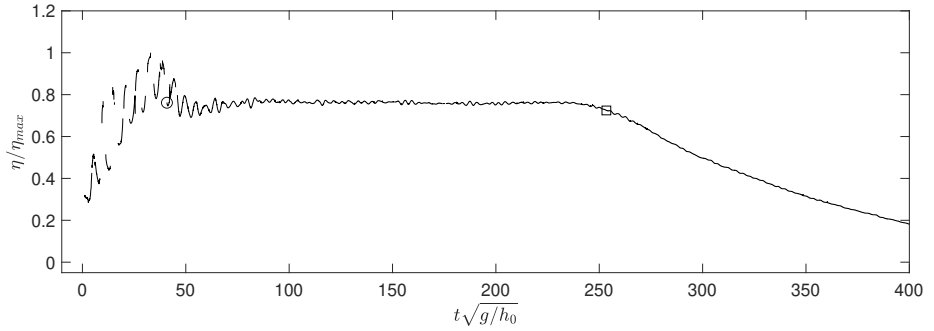

FIGURE S10. Time history of normalized free surface elevation at the still water shoreline for $L_r/h_0 = 176$ and $F_{in} = 1.3$. The circle and the square markers represent the beginning and end of the bore plateau.

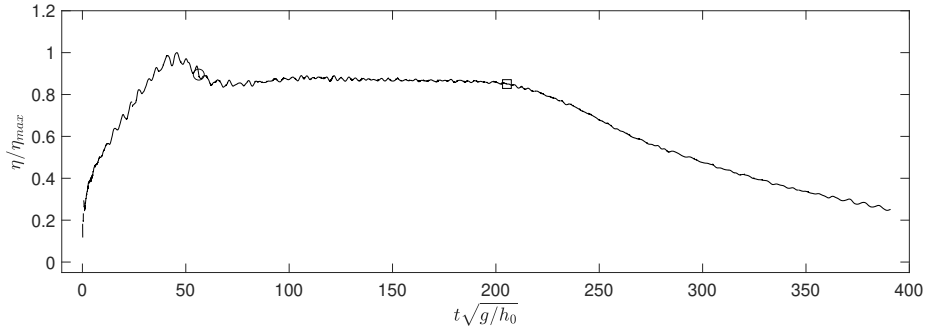

FIGURE S11. Time history of normalized free surface elevation at the still water shoreline for $L_r/h_0 = 176$ and $F_{in} = 1.5$. The circle and the square markers represent the beginning and end of the bore plateau.

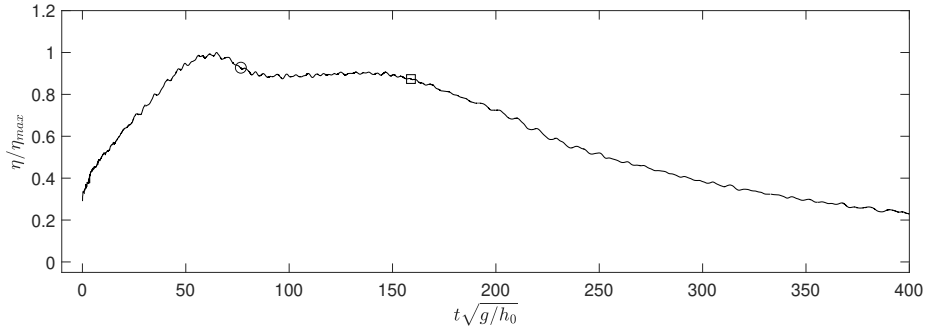

FIGURE S12. Time history of normalized free surface elevation at the still water shoreline for $L_r/h_0 = 176$ and $F_{in} = 1.9$. The circle and the square markers represent the beginning and end of the bore plateau.

the comparison between the laboratory measurements and numerical results, $\delta = 0.8$ is chosen to model the wave breaking accurately for $\Delta x = 0.02$ m.

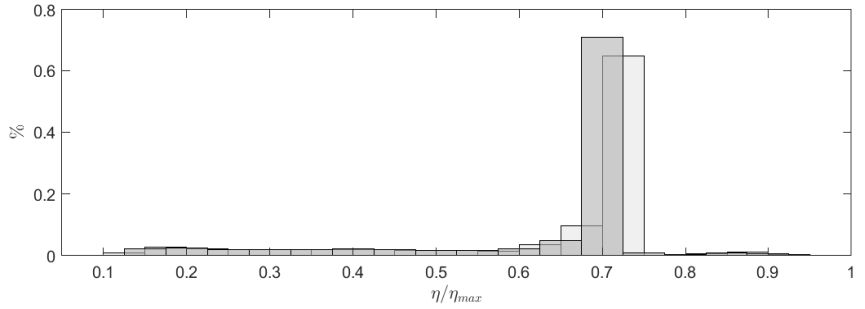

FIGURE S13. Histogram of normalized free surface elevations at the still water shoreline (figure S9) for $L_r/h_0 = 176$ and $F_{in} = 1.1$.

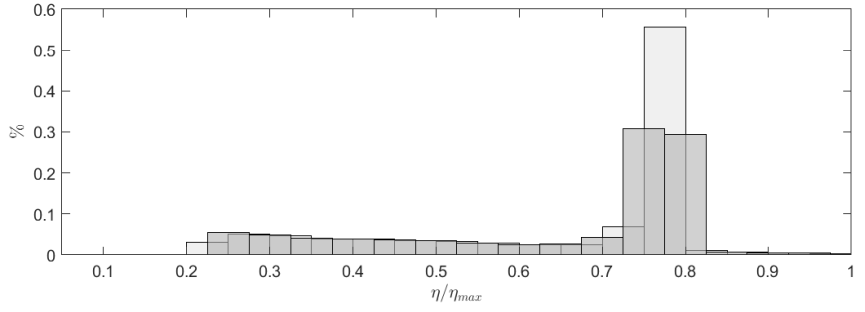

FIGURE S14. Histogram of normalized free surface elevations at the still water shoreline (figure S10) for $L_r/h_0 = 176$ and $F_{in} = 1.3$.

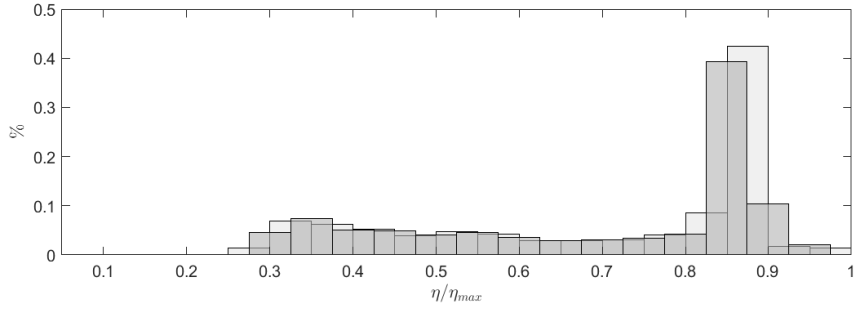

FIGURE S15. Histogram of normalized free surface elevations at the still water shoreline (figure S11) for $L_r/h_0 = 176$ and $F_{in} = 1.5$.

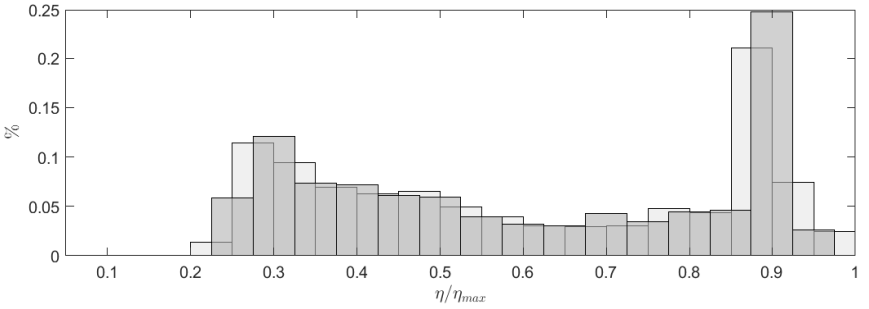

FIGURE S16. Histogram of normalized free surface elevations at the still water shoreline (figure S12) for $L_r/h_0 = 176$ and $F_{in} = 1.9$.

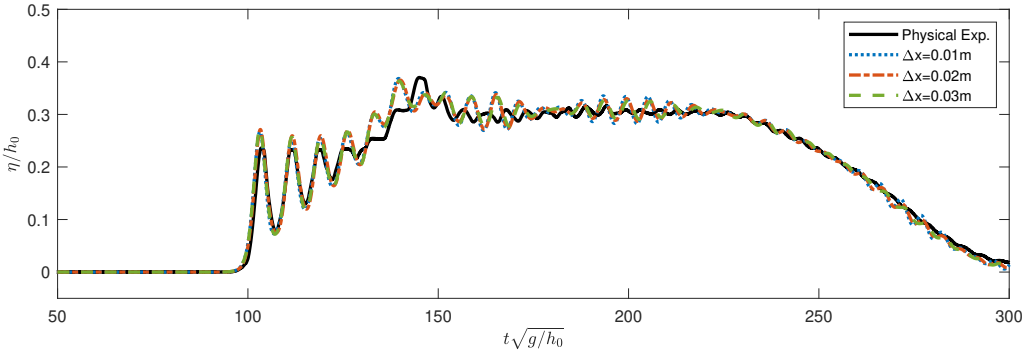

FIGURE S17. Dimensionless free surface elevation at the toe of the slope for $F_{in} = 1.1$. The steepness value $\delta = 0.8$ is used.

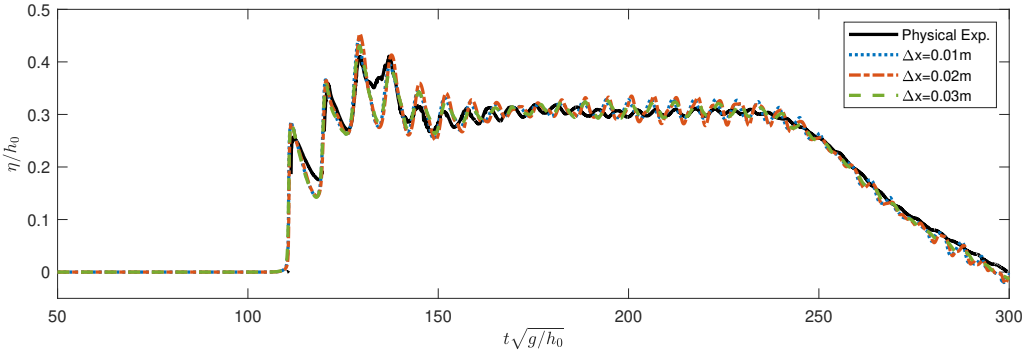

FIGURE S18. Dimensionless free surface elevation at the still shoreline for $F_{in} = 1.1$. The steepness value $\delta = 0.8$ is used.

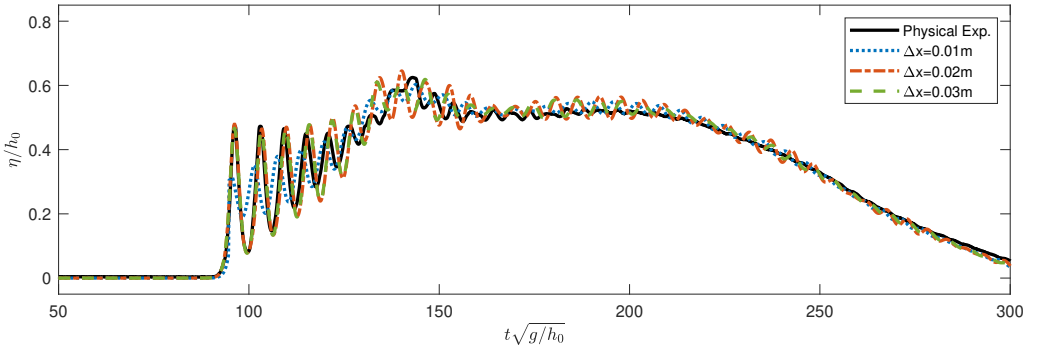

FIGURE S19. Dimensionless free surface elevation at the toe of the slope for $F_{in} = 1.2$. The steepness value $\delta = 0.8$ is used.

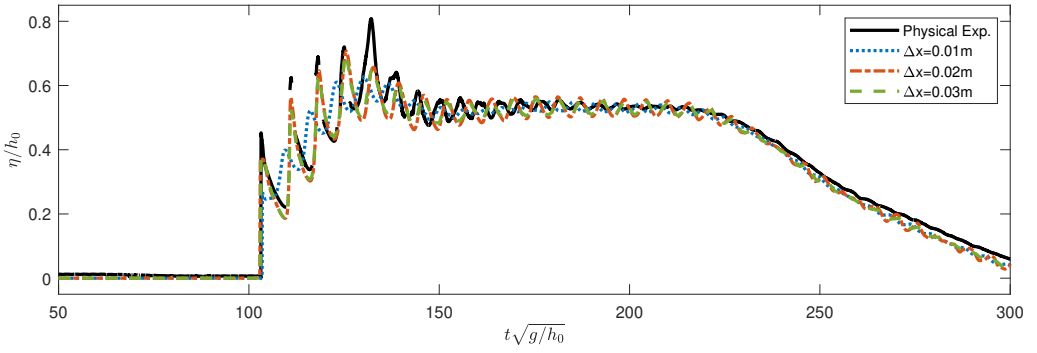

FIGURE S20. Dimensionless free surface elevation at the still shoreline for $F_{in} = 1.2$. The steepness value $\delta = 0.8$ is used.

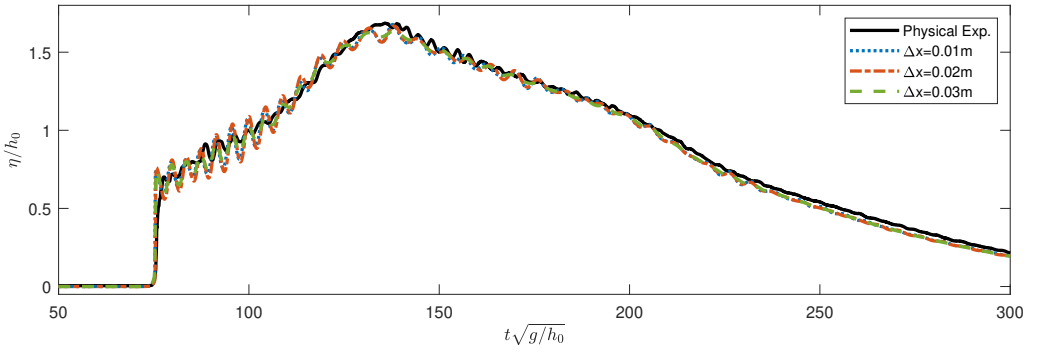

FIGURE S21. Dimensionless free surface elevation at the toe of the slope for $F_{in} = 1.5$. The steepness value $\delta = 0.8$ is used.

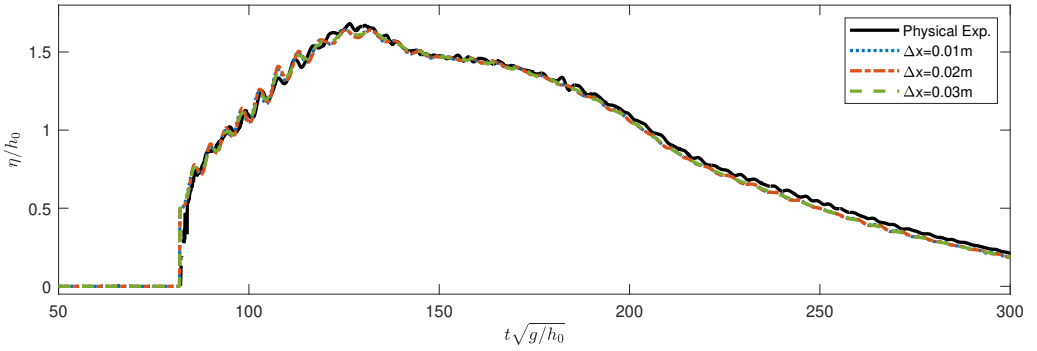

FIGURE S22. Dimensionless free surface elevation at the still shoreline for $F_{in} = 1.5$. The steepness value $\delta = 0.8$ is used.

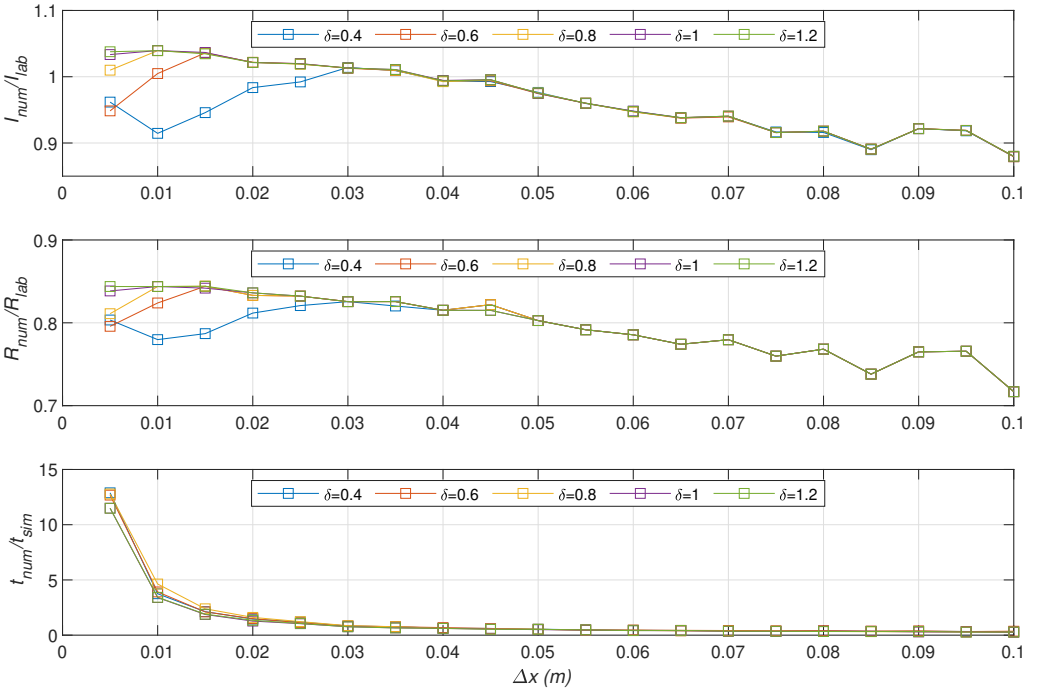

FIGURE S23. The ratio of the numerical solution for the maximum inundation, I_{num}, and the corresponding laboratory measurement, I_{lab}, at still water shoreline on the top panel; the ratio of numerical solutions for the runup, R_{num}, and the corresponding laboratory measurement, R_{lab} on the center panel; and the ratio of the time necessary to carry out the simulation, t_{num}, and the simulation duration, t_{sim}, on the bottom panel versus grid size Δx for $F_{in} = 1.1$.

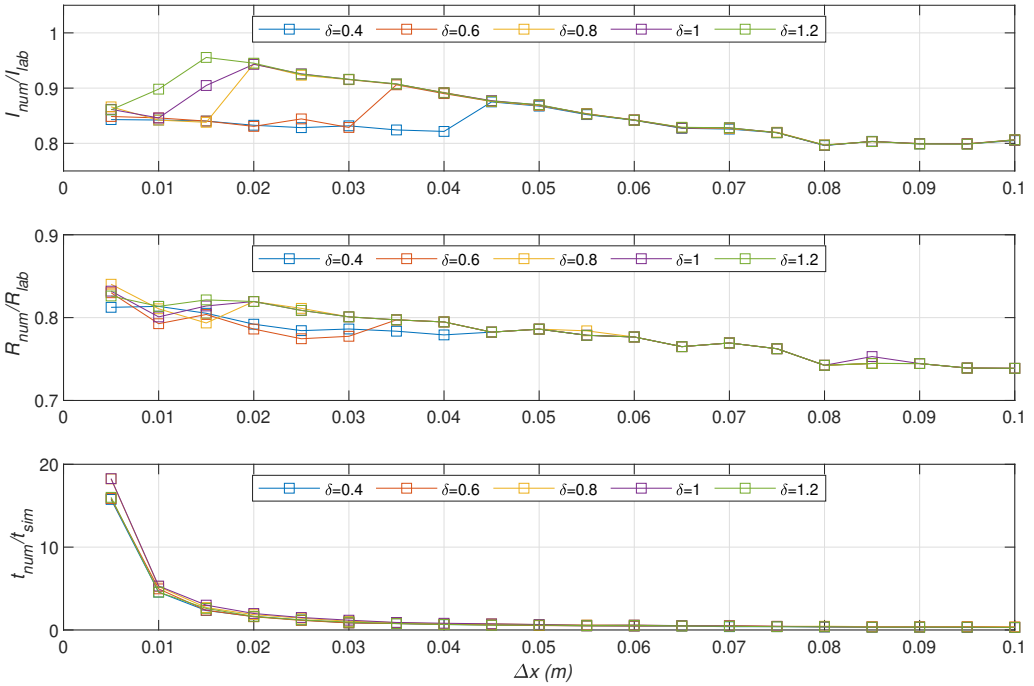

FIGURE S24. The ratio of the numerical solution for the maximum inundation, I_{num}, and the corresponding laboratory measurement, I_{lab}, at still water shoreline on the top panel; the ratio of numerical solutions for the runup, R_{num}, and the corresponding laboratory measurement, R_{lab} on the center panel; and the ratio of the time necessary to carry out the simulation, t_{num}, and the simulation duration, t_{sim}, on the bottom panel versus grid size Δx for $F_{in} = 1.2$.

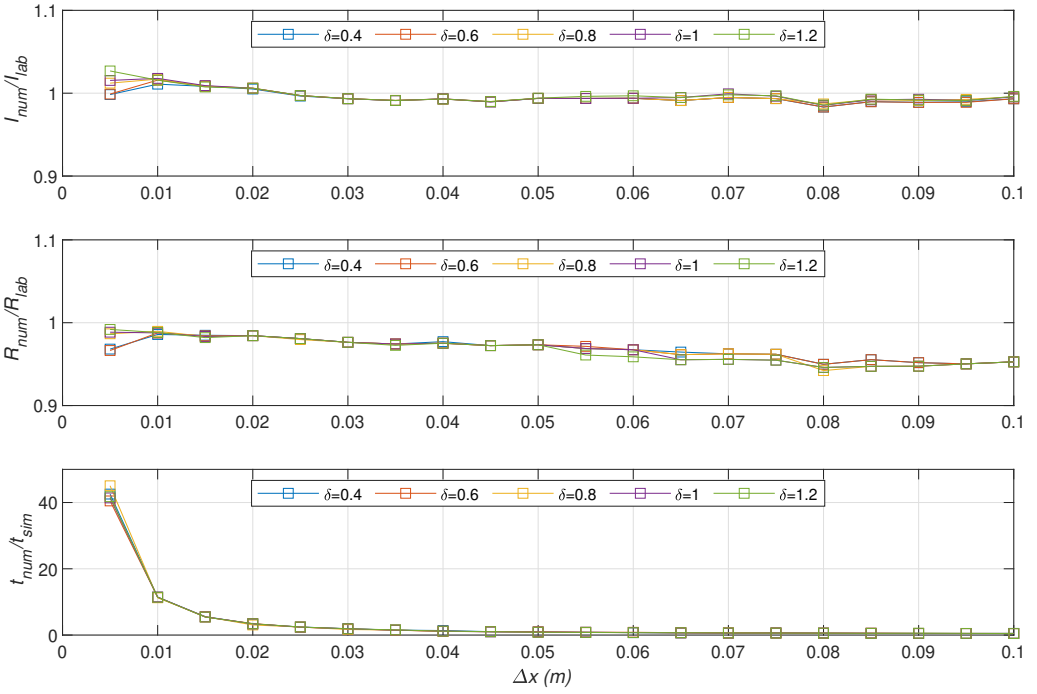

FIGURE S25. The ratio of the numerical solution for the maximum inundation, I_{num}, and the corresponding laboratory measurement, I_{lab}, at still water shoreline on the top panel; the ratio of numerical solutions for the runup, R_{num}, and the corresponding laboratory measurement, R_{lab} on the center panel; and the ratio of the time necessary to carry out the simulation, t_{num}, and the simulation duration, t_{sim}, on the bottom panel versus grid size Δx for $F_{in} = 1.5$.